UC Irvine

UC Irvine Previously Published Works

Title

A study on intermetallic compound formation in Ag–Al system and evaluation of its mechanical properties by micro-indentation

Permalink

https://escholarship.org/uc/item/2j52k4cr

Journal

Journal of Materials Science: Materials in Electronics, 29(5)

ISSN

0957-4522

Authors

Fu, Shao-Wei
Lee, Chin C

Publication Date

2018-03-01

DOI

10.1007/s10854-017-8340-1

Peer reviewed

eScholarship.org Powered by the California Digital Library
University of California

Journal of Materials Science: Materials in Electronics (2018) 29:3985–3991
https://doi.org/10.1007/s10854-017-8340-1

A study on intermetallic compound formation in Ag–Al system and evaluation of its mechanical properties by micro-indentation

Shao-Wei Fu[1] · **Chin C. Lee**[1]

Received: 25 July 2017 / Accepted: 27 November 2017 / Published online: 29 November 2017
© Springer Science+Business Media, LLC, part of Springer Nature 2017

Abstract
In electronic packaging in recent years, silver (Ag) alloy wires have been widely adopted in wire-bond processes. The bond pads on the device chips are mostly aluminum (Al). Thus, the bonding interface is mainly Ag–Al. In recent Ag alloy wire-bond publications, it is unclear what intermetallic phases form at the interface. In this research, experiments were designed to understand the Ag–Al intermetallic compound (IMC) formation in the Ag–Al system and evaluate its mechanical properties. First, the Ag–Al alloys with compositions from 19 to 43 at.% Al were evaluated to identify the phase equilibrium and crystal structure of the Ag–Al intermetallic phases. Microstructures and phase compositions of the designed Ag–Al alloys are presented. To further study the intermetallic compound formation at the Ag/Al interface, the interfacial reaction of the Ag/Al joints at 200 °C was investigated. The μ-Ag_3Al and δ-Ag_2Al IMC were identified to form at the Ag/Al interface and stabilize after long-time annealing at 200 °C. At last, deformation and fracture behaviors of the bulk μ-Ag_3Al and δ-Ag_2Al were analyzed by the micro-indentation. The measured results reveal that μ-Ag_3Al exhibits significantly higher hardness and lower fracture toughness as compared to δ-Ag_2Al. Indentation crack propagation in μ-Ag_3Al demonstrates the fracture characteristics of brittle materials. In the case of δ-Ag_2Al, the presence of slip bands exhibits the ductility of δ-Ag_2Al to endure plastic deformation prior to fracture. The effect of the mechanical properties of the μ-Ag_3Al and δ-Ag_2Al IMC on the Ag–Al joint reliability is discussed. New information obtained in this research is important for future study of the joint reliability and failure mechanism of Ag–Al wire bonds.

1 Introduction

Wire bonding technology has been widely used to interconnect chips and substrates of microelectronic packages [1–3]. In the 1980s, both aluminum (Al) and gold (Au) wires were adopted in wire bonding. With increasing demand for high complexity and high reliability packaging, thermosonic ball bonding with Au wires became the dominant wire bonding technique. As the pitch of wire bonds continued to decrease, Al wires were abandoned because of their rapid oxide growth during spark ball formation. However, large diameter Al wires are still used on high power devices with the wedge bonding method [4]. Au wire diameter has continued to decrease to 15 μm due to rising gold prices and shrinking pad size [5, 6]. On the other hand, the rising gold price has motivated the packaging industry to look for alternative wire materials such as silver (Ag) and copper (Cu) [7–11]. Recently, several packaging companies have bonded Cu wires on Al bond-pads in production. The Cu/Al interface reaction and Cu wire bond reliability have been reported [7, 8]. Since Cu wires get oxidized easily and exhibit higher hardness as compared to Au and Ag alloy wires, Cu wires possess a narrower process window for wire bonding. The high hardness of Cu could cause Al pads splashing, and the higher bonding force for Cu wire bonding could induce Si chip cratering [9]. In addition, Cu-Al wire bonds exhibit low corrosion resistance to halogen elements under high humidity. Halogen content, such as chlorine, in molding compound should be controlled to prevent the corrosion at the Cu/Al interface [11].

Recently, Ag alloy wires have been introduced as a new bonding wire alternative [10, 12]. Compared to Cu wires, Ag alloy wires have the advantages of higher oxidation resistance and higher ductility. Thus, Ag alloy wire bonding exhibits a wider process window and can reduce Al pad splash and silicon damage [13]. A concern is intermetallic

✉ Shao-Wei Fu
shaoweif@uci.edu

[1] Electrical Engineering and Computer Science, Materials and Manufacturing Technology, University of California, Irvine, CA 92697-2660, USA

compound (IMC) formation at the bonding interface. The IMC layer has often been found to be the weak region due to its brittle nature, leading to a high failure rate of the bonding joints [14–17]. Several research studies have sought to understand the IMC formation and the resulting phases in Ag–Al wire bonds. However, the Ag–Al IMC phases reported are not conclusive. One research group indicated Ag_4Al and Ag_2Al phases [18] and others showed $AgAl_2$, Ag_2Al and Ag_3Al phases at the Ag/Al interface [19, 20]. Moreover, although many studies have reported the reliability test results of the Ag–Al wire bonds [18–21], the mechanical properties of the Ag–Al intermetallics are still unclear.

Therefore, this study aims to investigate the Ag–Al intermetallic compound formation in Ag–Al system and further evaluate its mechanical properties. First, the Ag–Al alloys with compositions from 19 to 43 at.% Al were evaluated to identify the phase equilibrium and crystal structure of the Ag–Al intermetallic phases. By studying the interfacial reaction of the Ag/Al joints, μ-Ag_3Al and δ-Ag_2Al IMC were identified to form at the Ag/Al interface and stabilize after long-time annealing at 200 °C. Finally, deformation and fracture behaviors of the bulk μ-Ag_3Al and δ-Ag_2Al were analyzed by the micro-indentation. Mechanical properties of the μ-Ag_3Al and δ-Ag_2Al were probed and discussed.

2 Experimental procedures

Ag–Al alloy ingots were grown through the casting method followed by long-time annealing. Ag and Al shots with 99.99% purity were uniformly mixed and loaded into 150 mm long quartz tubes with 1 cm in inner diameter. After loading, the tubes were evacuated by a vacuum pump and sealed by a hydrogen torch to form capsules. The capsules were brought to and kept at 1000 °C for 2 h, followed by 48-h annealing at 50 °C above the liquidus temperature to ensure complete homogenization. The sealed samples were then water quenched to room temperature to avoid excess phase formation during the cooldown process. Subsequently, solid-state annealing was performed at 200 °C for up to 750 h. After annealing, the ingots (40–45 mm long and 10 mm in diameter) were cut into disks with a thickness of 1 mm and mechanically polished for further examination. The casted ingot and disk samples after annealing are shown in Fig. 1. Chemical compositions, microstructures, and crystal structures of the disk specimens were characterized by a scanning electron microscope with energy dispersive X-ray spectroscopy (SEM/EDX, Philips XL-30 FEG SEM) and X-ray diffraction (XRD, Rigaku Smartlab X-ray diffractometer).

To further study the intermetallic compound formation at the Ag/Al interface, the interfacial reaction of the Ag/Al joints at 200 °C was investigated in this study. Ag–Al joints were prepared by bonding Ag disks to Al substrates using the solid-state bonding process. The bonding process was performed at 350 °C with a 1000 psi (6.89 MPa) static pressure for 450 s in the 0.1 torr vacuum. Subsequently, the Ag–Al joints were annealed at 200 °C for 750 h to form the Ag–Al IMC layer. To avoid possible damaging from the conventional mechanical polishing process, the cross-sectional Ag/Al joint specimens were prepared by the using focused ion beam milling technique. The interfacial morphologies and the phase compositions were evaluated by SEM/EDX.

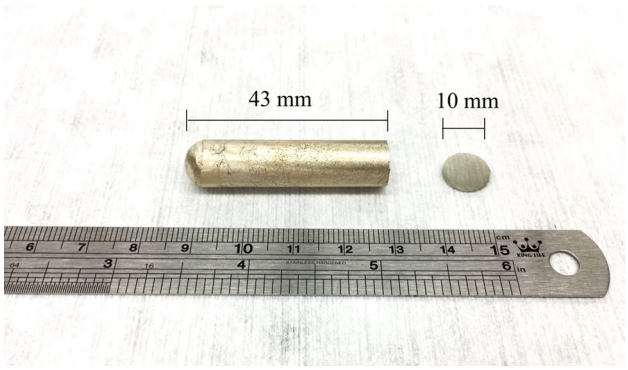

Fig. 1 The casted ingot and disk samples after annealing at 200 °C for 750 h. After annealing, the ingot samples were cut into disks (10 mm in diameter and 1 mm in thickness) and mechanically polished for further examination

After identifying the intermetallic compound formation in the Ag–Al alloys and Ag/Al joints, the mechanical properties of the two stable intermetallic phases, μ-Ag_3Al and δ-Ag_2Al, were studied. The hardness, elastic modulus and fracture toughness of bulk μ-Ag_3Al and δ-Ag_2Al were analyzed by a micro-hardness tester (Buehler, Lake Bluff, IL Micromet II Micro Hardness Tester). Vickers indentation mode was used with indentation loads ranging between 100 and 1000 gf. SEM observations were conducted after indentation to determine the average lengths of the induced cracks.

3 Results and discussions

In order to understand Ag–Al binary system and study the equilibrium Ag–Al intermetallic phases, the Ag–Al phase diagrams [22–24] are reviewed. In Fig. 2, we put the experimental phase diagram [22] and two calculated phase diagrams [23, 24] together for comparison. Below 873 k (600 °C), all three phase diagrams indicate that there are only two intermetallic phases, δ-Ag_2Al and μ-Ag_3Al. The experimental and calculated boundaries of the δ-Ag_2Al phase are in good agreement. However, the experimental and calculated boundaries of the μ-Ag_3Al phase differ

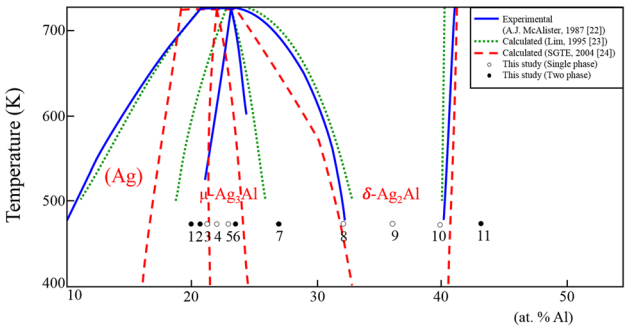

Fig. 2 Experimental [22] and calculated [23, 24] Ag–Al phase diagrams from 10 to 50 at.% Al at 400 to 725 K. The solid lines and dashed lines represent experimental data and calculated data, respectively. Spots marked 1–11 reveal the equilibrium phases identified in Ag–Al alloy samples no. 1 to no. 11 with composition from 19 to 43 at.% Al, as shown in Table 1. The white spot indicates a phase from a single-phase sample. The black spot is a phase from a two-phase alloy

significantly. Below 523 k (250 °C), the crystal structures and boundaries of μ-Ag_3Al and δ-Ag_2Al phases are sparse and incomplete. In industry, the temperature range between 125 and 300 °C has been chosen for the standard thermal storage testing of wire bonds, and the temperature range between 150 and 250 °C is the typical post-mold curing process [25]. It is critical to understand the equilibrium intermetallic phase in the Ag–Al system within this temperature range and further study its crystal structure and mechanical properties. In this study, eleven alloys with compositions from 19 to 43 at.% Al annealed at 200 °C were employed to obtain two single-phase intermetallic phases and three mixed-phase alloys, as listed in Table 1. The experimental results show that both intermetallic phases, μ-Ag_3Al and δ-Ag_2Al, stabilize at 200 °C after long-time annealing. In Fig. 2, the white spots represent a single-phase intermetallic in the sample. The black spots represent a two-phase alloy in the sample. At 200 °C, single-phase μ-Ag_3Al stabilizes in the composition range from 21.6 to 22.9 at.% Al, and single-phase δ-Ag_2Al stabilizes in the composition range from 32.1 to 39.9 at.% Al. In addition, three two-phase alloys, μ-Ag_3Al + (Ag), μ-Ag_3Al + δ-Ag_2Al, and δ-Ag_2Al + (Al), were produced and studied.

In the following section, microstructures and crystal structures of the Ag–Al alloys are presented. Figure 3 exhibits the SEM back-scattered electron images of the representative Ag–Al alloys, including single-phase intermetallics, μ-Ag_3Al and δ-Ag_2Al, and two-phase alloys, μ-Ag_3Al + (Ag), μ-Ag_3Al + δ-Ag_2Al, and δ-Ag_2Al + (Al). Figure 4 displays the corresponding XRD spectra of the Ag–Al alloys. Results show that single-phase μ-Ag_3Al remains as the cubic structure (A13, β-Mn type) when stabilized at 200 °C, and the single-phase δ-Ag_2Al exhibits the hexagonal structure (A3, Mg type) when stabilized at 200 °C. SEM images of the homogeneous μ-Ag_3Al and δ-Ag_2Al are presented in Fig. 3a, b. Microstructures of the two-phase alloys, Ag-19 at.% Al alloy, Ag-27 at.% Al alloy and Ag-43 at.% Al alloy, are shown in Fig. 3c–f. In the Ag-19 at.% Al alloy, it is observed that the brighter (Ag) strips are embedded in the μ-Ag_3Al phase. The Al solubility detected in (Ag) solid solution is approximately 15.5 at.%. The Ag-27 at.% Al alloy exhibits a mixed-phase with μ-Ag_3Al and δ-Ag_2Al intermetallics, as shown in Fig. 3d. The brighter phase is the μ-Ag_3Al phase with 22.8 at.% Al, and the darker phase is the δ-Ag_2Al phase with 31.9 at.% Al. Figure 3e, f exhibit the hypoeutectic microstructures of the Ag-43 at.% Al alloy. The microstructure is formed by the oval-shaped δ-Ag_2Al grains surrounded by the dark intergranular (Al) phase with fine precipitates. The needle-shaped precipitates in (Al) phase, as shown in Fig. 3f, are identified as the δ-Ag_2Al phase by EDX. The Ag concentration detected in (Al) solid solution is approximately 2.2 at.%. The precipitation of the needle-shaped δ-Ag_2Al in (Al) phase is attributed to the decreased Ag solubility in (Al) phase from liquidus temperature to 200 °C. The over-saturated Ag in (Al) phase leads to the formation of

Table 1 Equilibrium phase and chemical compositions of the observed Ag–Al alloys as determined in present study

#	Designed alloy compositions	Microstructure	Chemical compositions	Phases
1	Ag-19 at.% Al	Two-phase	(Ag-15.5 at.% Al) + (Ag-21.5 at.% Al)	(Ag) + μ-Ag_3Al
2	Ag-21 at.% Al	Two-phase	(Ag-15.4 at.% Al) + (Ag-21.7 at.% Al)	(Ag) + μ-Ag_3Al
3	Ag-21.5 at.% Al	Single phase	Ag-21.6 at.% Al	μ-Ag_3Al
4	Ag-22 at.% Al	Single phase	Ag-22.0 at.% Al	μ-Ag_3Al
5	Ag-23 at.% Al	Single phase	Ag-22.9 at.% Al	μ-Ag_3Al
6	Ag-23.5 at.% Al	Two-phase	(Ag-22.9 at.% Al) + (Ag-32.0 at.% Al)	μ-Ag_3Al + δ-Ag_2Al
7	Ag-27 at.% Al	Two-phase	(Ag-22.8 at.% Al) + (Ag-31.9 at.% Al)	μ-Ag_3Al + δ-Ag_2Al
8	Ag-32 at.% Al	Single phase	Ag-32.1 at.% Al	δ-Ag_2Al
9	Ag-36 at.% Al	Single phase	Ag-35.8 at.% Al	δ-Ag_2Al
10	Ag-40 at.% Al	Single phase	Ag-39.9 at.% Al	δ-Ag_2Al
11	Ag-43 at.% Al	Two-phase	(Al-2.2 at.% Ag) + (Ag-39.8 at.% Al)	(Al) + δ-Ag_2Al

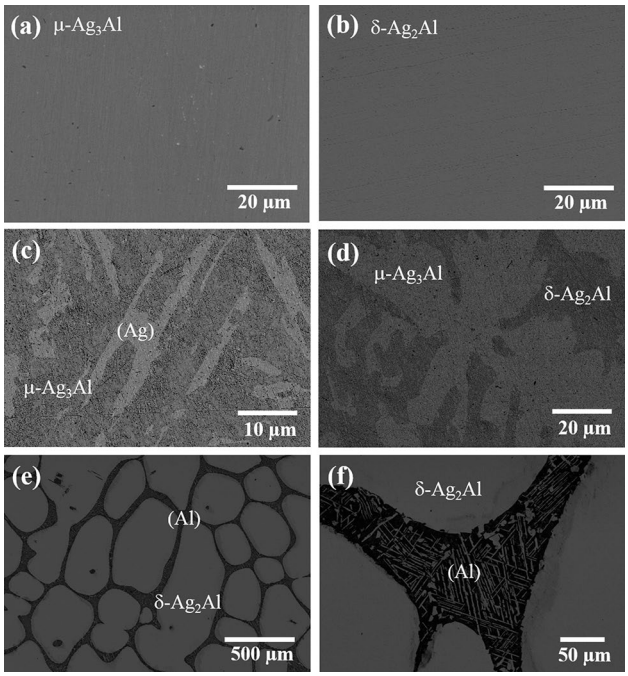

Fig. 3 Back-scattered SEM images showing microstructures of Ag–Al alloys. The single-phase intermetallics **a** Ag-36 at.% Al and **b** Ag-22 at.% Al. The two-phase alloys **c** Ag-19 at.% Al alloy, **d** Ag-27 at.% Al alloy, and **e** Ag-43 at.% Al alloy. **f** shows the enlarged area of (**e**). Phases identified for each sample are indicated on the image and listed in Table 1

secondary δ-Ag_2Al precipitates inside the (Al) solid solution phase as annealing at 200 °C. The XRD spectra of the two-phase alloys, Ag-19 at.% Al alloy, Ag-27 at.% Al alloy, and Ag-43 at.% Al alloy, are shown in Fig. 4 (c) to (e).

The results above reveal that the Ag–Al intermetallic phases, μ-Ag_3Al and δ-Ag_2Al, can stabilize and coexist with (Ag) or (Al) in Ag–Al alloys after long-time annealing at 200 °C. To further study the Ag–Al intermetallic compound formation at the Ag/Al interface, the interfacial reaction of the Ag/Al joints at 200 °C was investigated. The Ag–Al joints were prepared by bonding Ag disks to Al substrates using the solid-state bonding process. Figure 5 shows the microstructure of the Ag–Al joints after annealing at 200 °C for 750 h. On the cross-sectional SEM image, red dots marked 1–5 indicate the EDX analysis location on the interface region. The resulting phase compositions are listed in the table below. During solid-state reaction at 200 °C, the atomic inter-diffusion of Ag and Al leads to the Ag–Al IMC formation at the joint interface. The microstructure shows the Ag–Al IMC grew into both Al and Ag sides from the joint interface. From the EDX results, the scallop-type IMC which grew into the Al side was identified as δ-Ag_2Al. The layer-type IMC which grew into the Ag side was characterized as δ-Ag_2Al and μ-Ag_3Al, while the μ-Ag_3Al IMC layer was detected between the δ-Ag_2Al IMC and the Ag region.

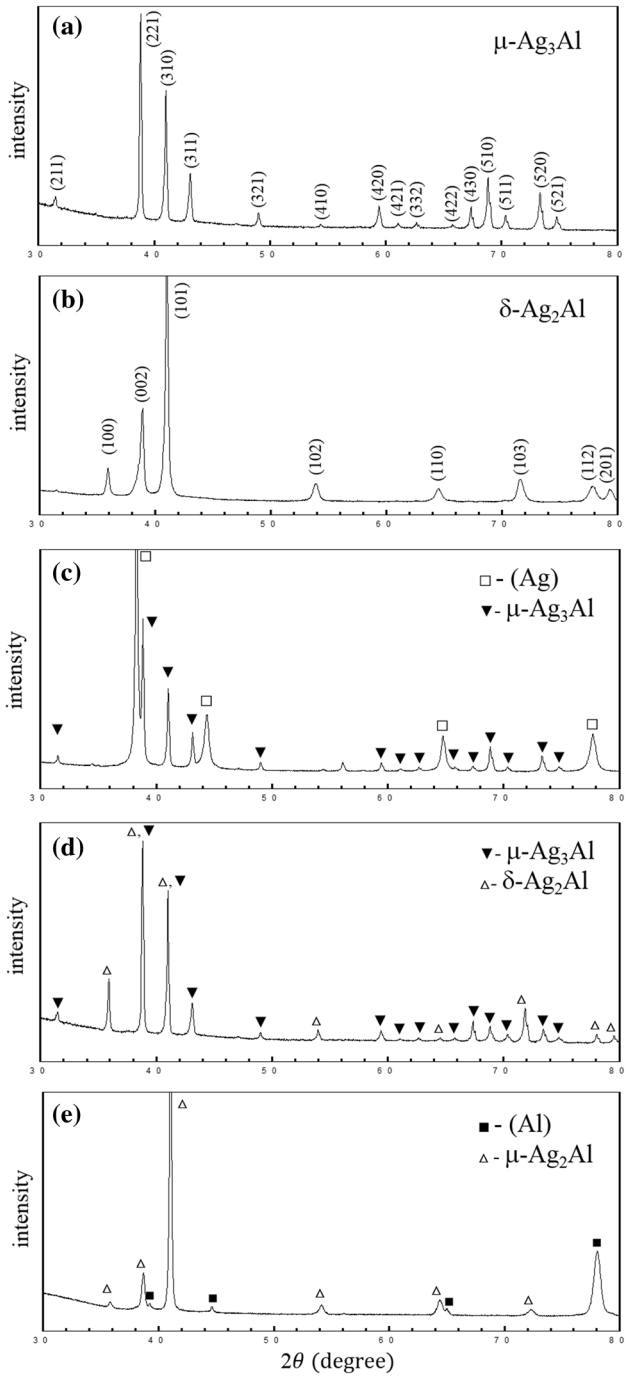

Fig. 4 XRD spectra of the representative Ag–Al alloys **a** Ag-36 at.% Al, **b** Ag-22 at.% Al, **c** Ag-19 at.% Al alloy, **d** Ag-27 at.% Al alloy, and **e** Ag-43 at.% Al alloy

As shown in the table below, at the Ag/Al interface, the δ-Ag_2Al IMC on region 2 and 3 exhibits similar compositions, containing approximately 34.5 at.% Al. The μ-Ag_3Al IMC layer contains 22.1 at.% Al.

As reported above, after annealing the Ag–Al alloys and the Ag–Al joints at 200 °C, the phase equilibrium and crystal

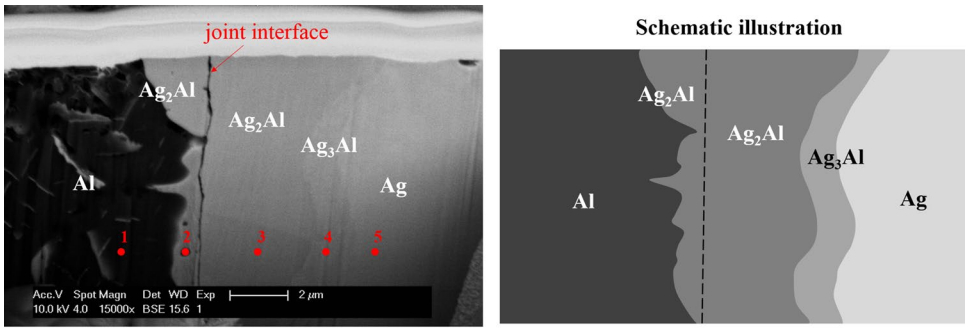

Fig. 5 The cross-sectional SEM image of the Ag–Al joints after annealing at 200 °C for 750 h. Red dots marked 1–5 indicate the EDX analysis location on the interface region. The resulting phase compositions are listed in the table below

	Ag (at.%)	Al (at.%)	Remark
Region 1	0.9	99.1	Al
Region 2	65.5	34.5	Ag_2Al
Region 3	65.7	34.3	Ag_2Al
Region 4	77.9	22.1	Ag_3Al
Region 5	98.3	1.7	Ag

structures of the Ag–Al intermetallics are demonstrated. The Ag–Al joints were examined to study the IMC microstructure at the Ag/Al interface. In the industrial Ag–Al wire bonding process, bonding parameters such as electronic flame off (EFO) process and ultrasonic power could affect the Ag–Al interdiffusion and IMC nucleation at the bonding interface. Therefore, the Ag–Al IMC phases reported at the Ag–Al wire bonds interface are not conclusive. In this study, after long-term annealing the Ag–Al joints, δ-Ag_2Al and μ-Ag_3Al were identified as the thermodynamically stable phases at the Ag/Al interface. The thickness of δ-Ag_2Al and μ-Ag_3Al IMC layers in the Ag–Al joint is approximately 2–5 μm, which is in a comparable range to the IMC growth in Ag–Al wire bonds. Since the IMC layer is considered as the weak region within the wire bonds and could lead to brittle failure of the joint, it is important to understand the mechanical properties of the Ag–Al IMCs.

To investigate the mechanical properties of Ag–Al IMCs, the hardness and fracture toughness of the μ-Ag_3Al and δ-Ag_2Al were analyzed by the micro-indentation. Instead of using Ag–Al joints, bulk μ-Ag_3Al and δ-Ag_2Al were prepared as the indentation specimens to achieve larger analysis area for Ag–Al IMCs and avoid interface defect in Ag–Al joints. Single-phase μ-Ag_3Al with 22.0 at.% Al and δ-Ag_2Al with 35.8 at.% Al were produced. The polished intermetallics were analyzed by a Vickers indenter using a loading force ranging between 100 and 1000 gf. The characteristic features of indentation deformation and cracks in bulk μ-Ag_3Al and δ-Ag_2Al are shown in Fig. 6. The hardness (H), elastic modulus (E), and fracture toughness (K_{1C}) of μ-Ag_3Al and δ-Ag_2Al are listed in Table 2. Bulk μ-Ag_3Al exhibits significantly higher hardness than bulk δ-Ag_2Al and possesses fracture toughness value of 1.61 ± 0.13 MPa$\sqrt{\text{m}}$. The fracture toughness value is calculated by the equation [26]:

$$K_{1C} = 0.016 \times \left(\frac{E}{H}\right)^{1/2} \frac{P}{c^{3/2}}$$

where c implies the length from the center of the contact to the end of the crack, P is the loading force, H is the measured hardness, and E is the measured elastic modulus. Figure 6a, b show the indentation cracks in bulk μ-Ag_3Al under a load of 300 gf and 500 gf. It is clearly observed that cracks emanated from all four corners of the indent in μ-Ag_3Al. At a higher load of 500 g, larger indent deformation and the longer cracks were detected in μ-Ag_3Al. It is clear that the indentation crack propagation in μ-Ag_3Al demonstrates the fracture characteristics of brittle materials. In the case of bulk δ-Ag_2Al, indentation cracks could not be induced after applying loads up to 1000 gf, as shown in Fig. 6c, d. With higher indent load, the extent of plastic deformation increases as indicated by the presence of slip bands around the indent. At a load of 1000 gf, parallel slip bands of about 10–20 μm wide formed in δ-Ag_2Al, as shown in Fig. 6d. Region A shows the slip bands nearly parallel to the indent edge, and region B and C reveal the coarser slip bands connected to the indent edge with an identical orientation. The formation of slip bands is attributed to the plastic deformation induced by the localized stress around the indent. The presence of slip bands exhibits the ability of δ-Ag_2Al to endure plastic deformation before fracture. These microstructures imply the significant intrinsic ductility of δ-Ag_2Al intermetallic.

As a result, among two Ag–Al intermetallics, μ-Ag_3Al demonstrates the brittle fracture characteristics in the micro-indentation analysis. The measured results reveal that μ-Ag_3Al exhibits significantly higher hardness and lower fracture toughness as compared to δ-Ag_2Al. Therefore, the formation of interfacial μ-Ag_3Al IMC could lead to brittle fracture at the Ag–Al wire bonding interface and

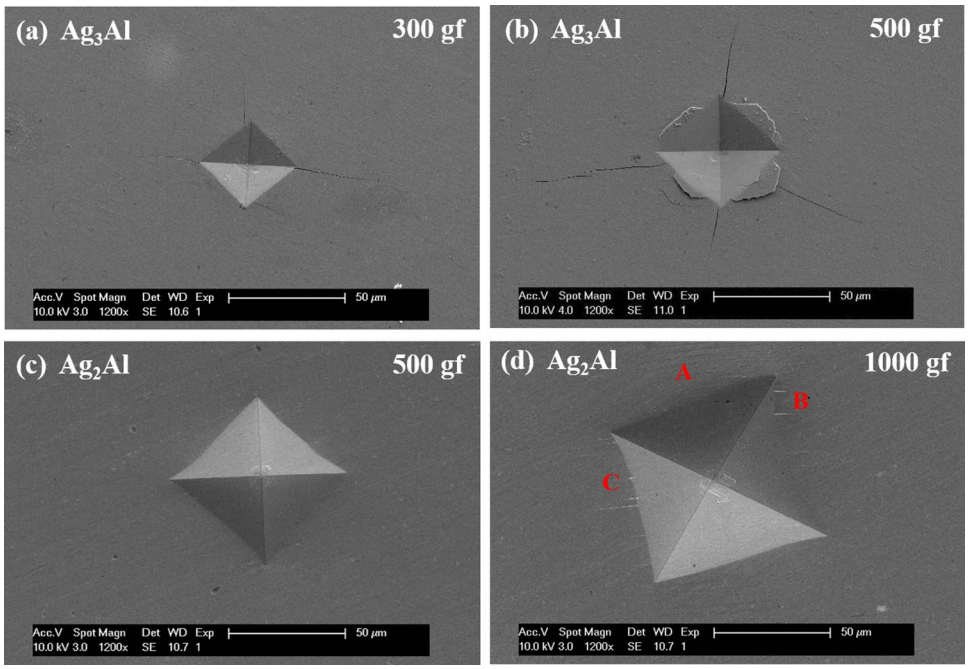

Fig. 6 Indentation deformation and cracks morphology in **a** bulk μ-Ag_3Al under loading of 300 gf and **b** 500 gf, and **c** bulk δ-Ag_2Al under loading of 500 gf and **d** 1000 gf. In sample **d**, region A, B and C show the presence of slip bands around the indent

Table 2 Phase compositions, hardness (*H*), elastic modulus (*E*), and fracture toughness (*Kc*) of the μ-Ag_3Al and δ-Ag_2Al

Phase	Composition	Hardness (MPa)	Elastic modulus (GPa)	Fracture toughness ($MPa\sqrt{m}$)
μ-Ag_3Al	Ag-22 at.% Al	2207 ± 141	110 ± 2.5	1.61 ± 0.13
δ-Ag_2Al	Ag-35.8 at.% Al	1222 ± 94	106 ± 2.1	–

degrade the joint reliability. Moreover, as crystal structures of μ-Ag_3Al and δ-Ag_2Al are demonstrated in this study, it is important to discuss the effect of lattice mismatch between the IMC phases and substrates on the Ag–Al joint reliability. In the Ag–Al system, δ-Ag_2Al with hexagonal structure and Al with face-centered-cubic form a well-lattice-matched δ-Ag_2Al/Al interface [27]. However, large lattice mismatch between the μ-Ag_3Al/Ag interface is expected due to the complex cubic structure of μ-Ag_3Al (A13, β-Mn type). In Ag–Al wire bonds, the large lattice mismatch between the μ-Ag_3Al and Ag could induce lattice strain and defects at the compound interface, decreasing the interfacial stability. Due to the brittle nature of μ-Ag_3Al and the large lattice mismatch at the μ-Ag_3Al/Ag interface, suppressing the formation of μ-Ag_3Al IMC is extremely important to enhance the Ag–Al joint reliability. For Ag-Al wire bonds, adding some elements to Ag wires might reduce the Ag–Al IMC growth or change the phase compositions of the Ag–Al IMC. Recently, Au and Pd elements have been added to produce Ag alloy wires. Ternary IMC phases, $(Ag, Pd)_2Al$, $(Ag, Pd)_3Al_2$ and $(Au,Ag)_4Al$, were probed at the Ag–Pd/Al and Ag–Au-Pd/Al interface [10, 28]. However, the crystal structures and mechanical properties of these ternary phases are still unclear.

4 Summary

In this study, experiments were established to investigate the Ag–Al IMC formation in Ag–Al system and evaluate its mechanical properties. First, the Ag–Al alloys of eleven compositions were grown and evaluated to identify the phase equilibrium and crystal structure of the Ag–Al intermetallic phases. Microstructures and phase compositions of the designed Ag–Al alloys are presented and discussed. The interfacial reaction of the Ag/Al joints at 200 °C was investigated. The μ-Ag_3Al and δ-Ag_2Al IMC were identified to form at the Ag/Al interface and stabilize after long-time annealing at 200 °C. Finally, deformation and fracture behaviors of the bulk μ-Ag_3Al and δ-Ag_2Al were analyzed by the micro-indentation. In μ-Ag_3Al, the indentation cracks propagation demonstrates the brittle fracture characteristics of μ-Ag_3Al. In δ-Ag_2Al, the absence of indentation cracks and observed slip bands imply the intrinsic ductility of δ-Ag_2Al. The measured results reveal that μ-Ag_3Al exhibits remarkably higher hardness and lower fracture toughness as compared to δ-Ag_2Al. Correlations between the mechanical properties of the Ag–Al IMC and the Ag–Al joint reliability are discussed. This research reveals the phase equilibrium and crystal structures of the Ag–Al IMCs and quantifies the intrinsic mechanical properties of μ-Ag_3Al and δ-Ag_2Al,

providing an important reference for securing the Ag–Al wire bonding reliability.

Acknowledgements SEM/EDX and XRD analysis were performed at the UC Irvine Materials Research Institute (IMRI). Micro-hardness analysis was conducted with the assistance of Steve Weinstock in department of Chemical Engineering and Materials Science at University of California, Irvine.

References

1. C. Harper, *Electronic Packaging and Interconnection Handbook*, (McGraw-Hill, Inc., New York, 2004)
2. E.R.R. Tummala, E.J. Rymaszewski, *Microelectronics Packaging Handbook*, (Springer, New York, 1997)
3. G.G. Harman, *Wire Bonding in Microelectronics*, (McGraw-Hill, New York, 2010)
4. A. Dasgupta, M. Pecht, Material failure mechanisms and damage models. IEEE Trans. Reliab. **40**(5), 531–536 (1991)
5. C. Breach, F. Wulff, New observations on intermetallic compound formation in gold ball bonds: general growth patterns and identification of two forms of Au 4 Al. Microelectron. Reliab. **44**(6), 973–981 (2004)
6. C. Breach, What is the future of bonding wire? Will copper entirely replace gold?. Gold Bull. **43**(3), 150–168 (2010)
7. C.L. Gan, U. Hashim, Evolutions of bonding wires used in semiconductor electronics: perspective over 25 years. J. Mater. Sci: Mater. Electron. **26**(7), 4412–4424 (2015)
8. Z. Zhong, Overview of wire bonding using copper wire or insulated wire. Microelectron. Reliab. **51**(1), 4–12 (2011)
9. B.K. Appelt, A. Tseng, C. Chen, Y. Lai, Fine pitch copper wire bonding in high volume production. Microelectron. Reliab. **51**(1), 13–20 (2011)
10. R. Guo, T. Hang, D. Mao, M. Li, K. Qian, Z. Lv, H. Chiu, Behavior of intermetallics formation and evolution in Ag–8Au–3Pd alloy wire bonds. J. Alloys Compd. **588**, 622–627 (2014)
11. C. Yu, C. Chan, L. Chan, K. Hsieh, Cu wire bond microstructure analysis and failure mechanism. Microelectron. Reliab. **51**(1), 119–124 (2011)
12. T. Chuang, C. Tsai, H. Wang, C. Chang, C. Chuang, J. Lee, H. Tsai, Effects of annealing twins on the grain growth and mechanical properties of Ag–8Au–3Pd bonding wires. J. Electron. Mater. **41**(11), 3215–3222 (2012)
13. C. Cheng, H. Hsiao, S. Chu, Y. Shieh, C. Sun, C. Peng, Low cost silver alloy wire bonding with excellent reliability performance, in *Electronic Components and Technology Conference (ECTC), 2013 IEEE 63rd* (2013), pp. 1569–1573
14. K. Sakuma, K. Sueoka, S. Kohara, K. Matsumoto, H. Noma, T. Aoki, Y. Oyama, H. Nishiwaki, P. Andry, C. Tsang, IMC bonding for 3D interconnection, in *Electronic Components and Technology Conference (ECTC), 2010 Proceedings 60th* (2010), pp. 864–871
15. Y.C. Jang, S.Y. Park, H.D. Kim, Y.C. Ko, K.W. Koo, M.R. Choi, H.G. Kim, N.K. Cho, I.T. Kang, J.H. Yee, Study of intermetallic compound growth and failure mechanisms in long term reliability of silver bonding wire, in *Electronics Packaging Technology Conference (EPTC), 2014 IEEE 16th* (2014), pp. 704–708
16. C. Lu, Review on silver wire bonding, in *Microsystems, Packaging, Assembly and Circuits Technology Conference (IMPACT), 2013 8th International* (2013), pp. 226–229
17. J. Xi, N. Mendoza, K. Chen, T. Yang, E. Reyes, S. Bezuk, J. Lin, S. Ke, E. Chen, Evaluation of Ag wire reliability on fine pitch wire bonding, in *Electronic Components and Technology Conference (ECTC), 2015 IEEE 65th* (2015), pp. 1392–1395
18. K. Yoo, C. Uhm, T. Kwon, J. Cho, J. Moon, Reliability study of low cost alternative Ag bonding wire with various bond pad materials, in *Electronics Packaging Technology Conference, EPTC'09, 11th* (2009), pp. 851–857
19. T. Chuang, C. Chang, C. Chuang, J. Lee, H. Tsai, Formation and growth of intermetallics in an annealing-twinned Ag–8Au–3Pd wire bonding package during reliability tests. IEEE Trans. Compon. Packag. Manuf. Technol. **3**(1), 3–9 (2013)
20. L.J. Kai, L.Y. Hung, L.W. Wu, M.Y. Chiang, D.S. Jiang, C. Huang, Y.P. Wang, Silver alloy wire bonding, in *Electronic Components and Technology Conference (ECTC), 2012 IEEE 62nd* (2012), pp. 1163–1168
21. M. Schneider-Ramelow, C. Ehrhardt, The reliability of wire bonding using Ag and Al. Microelectron. Reliab. **63**, 336–341 (2016)
22. A. McAlister, The Ag–Al (silver–aluminum) system. Bull. Alloy Phase Diagr. **8**(6), 526–533 (1987)
23. S. Lim, P. Rossiter, J. Tibballs, Assessment of the Al–Ag binary phase diagram. Calphad **19**(2), 131–141 (1995)
24. SGTE Binary Phase Diagram Collection. http://www.sgte.org
25. JESD22-A103E, *High Temperature Storage Life*, (JEDEC, Arlington, 2015)
26. D. Harding, W. Oliver, G. Pharr, Cracking during nanoindentation and its use in the measurement of fracture toughness. MRS Online Proc. Libr. Arch. **356**, 663 (1994)
27. S. Senapati, *Evolution of Lamellar Structures in Al–Ag Alloys*, (University of Central Florida, Orlando, 2005
28. W. Huang, K. Lin, Y. Lin, Y. Cheng, The intermetallic compound formation for the wire bond between an Al pad and Ag–xPd alloy wire. J. Electron. Mater. **45**, 6130–6136 (2016)